Progress In Electromagnetics Research, PIER 62, 281–315, 2006

ANALYSIS OF THE MIXED COUPLING IN BILATERAL MICROWAVE CIRCUITS INCLUDING ANISOTROPY FOR MICS AND MMICS APPLICATIONS

M. L. Tounsi, R. Touhami, and A. Khodja

Instrumentation Laboratory
Faculty of Electronics and Informatics
U.S.T.H.B University
P.O. 32, El-Alia, Bab-Ezzouar, 16111, Alger, Algeria

M. C. E. Yagoub

SITE, University of Ottawa
161, Louis Pasteur, Ottawa, ON, K1N 6N5, Canada

Abstract—Higher integration and smaller layout size, two major trends in today's industry, lead to more prominent electromagnetic coupling with direct applications in the RF/microwave area such as directional couplers, filters, multiplexers, shifters, delay lines, etc. In the present work, an efficient hybrid-mode method is presented for a rigorous characterization of the coupling in multilayer bilateral microwave circuits including anisotropy effects. Various types of planar configurations were considered including microstrip, finline and coplanar structures, but the proposed approach can easily be extended to any form of coupled lines. To fully characterize bilateral multilayer circuits in millimetre wave region with an arbitrary number of conductors, closed forms of dyadic Green's functions were determined in the spectral domain, with use of the Galerkin technique. The computed results show good agreement with data available in the literature. Furthermore, two original configurations based on three line bilateral couplers were computed and validated using neural network models.

1. INTRODUCTION

In RF/microwave circuits, transmission lines are usually used (i) to carry information or energy, and (ii) as circuit elements for passive

circuits like impedance transformers, filters, couplers, delay lines, resonators and baluns. Passive elements in conventional RF/microwave circuits employ transmission line sections and waveguides in different configurations, thereby achieving the desired functionality and meeting performance specifications. This functionality is largely achieved by the use of coupled transmission lines. In EM theory, the coupled power is function of the physical dimensions of the structure, the mode of propagation, the frequency of operation, and the direction of propagation of the primary power. Therefore, the various types of coupled-transmission line structures and the coupling mechanism must be accurately described.

In practice, one can distinguish between desired and undesired coupling. The first is intentionally used in coupled transmission structures with direct applications in coupler and filter circuit design, and equally important in the design of baluns, capacitors, inductors, transformers and dc blocks.

The second coupling, known as parasitic coupling, can take place in closely packed hybrid and monolithic integrated circuits, affecting the electrical performance of the circuit in several ways. It may change the frequency response in terms of frequency range and bandwidth and degrade the gain/insertion loss and its flatness, input and output voltage standing wave ratio (VSWR), and many other parameters such as output power, power-added efficiency, and noise figure.

This coupling can also result in the instability of an amplifier circuit and create a feedback resulting in a peak or a dip in the measured gain response or a substantial change in a phase-shifter response. In general, this parasitic coupling is undesirable and an impediment in obtaining an optimal solution in a circuit design.

Furthermore, multiconductor microstrip lines are widely used in very-large-scale integrated VLSI chips for digital applications and three-dimensional MICS. Here, numerous closely spaced interconnection lines in different planes are used to integrate the components in a chip. The design of these interconnections is very important to satisfy the size, power consumption, clock frequency and propagation delay requirements. Signal distortion, increases in background noise, and cross talk between the lines from coupling are some of the undesirable characteristics. Proper design of these interconnects can reduce the distortion and cross talk to acceptable levels and has played a significant role in the evolution of high-speed VLSI technology.

Therefore, an accurate circuit design cannot be performed without a rigorous characterization of all kind of coupling in multilayer bilateral microwave circuits. This can include anisotropic effects as well. To reach that target, the authors used the spectral domain approach

technique which makes use the Galerkin method to fully determine the coupling present in various types of bilateral planar circuits including microstrip, finline and coplanar structures which are very useful in the design of many microwave components for wireless communications.

Anisotropy is among the major trends in today's research [1–3] due to its numerous applications in particular to enhance certain circuit performances [4]. The existing theories developed for bilateral couplers [5–10] are limited to a fixed number of dielectric layers. In this work, the number of dielectric layers is arbitrary. Also, no symmetry is assumed in regards to the interface plane. An extension of the immittance approach technique [6] is presented to derive the dyadic admittance Green's functions for multilayered bilateral coupler structures via a recursive process, which allows a significant speed up of the CPU time. furthermore, the proposed approach is not restricted to the above configurations, but can be easily extended to any form of coupling between transmission lines. It was demonstrated through examples of passive structures including original configurations based on three line bilateral couplers. The computed data were validated using neural network models.

2. APPLICATIONS OF COUPLED PLANAR STRUCTURES

In the past decade, four major areas in development of coupled-line components have been emphasized: development of CAD tools, full-wave analysis and accurate semi-empirical expressions to enhance component designs, search for new structures and configurations and investigation for new applications. Broader bandwidths, ease of fabrication and integration, compact size, and lower cost, have been the driving factors. For example, in wireless applications, compact and lower cost requirements triggered investigation of new configurations and the transformation of existing structures into new layouts such as meander line and spiral to realize compact components. Other applications of coupled-line sections are in balun, impedance transformers, dc blocks interdigital capacitors, and spiral inductors. For instance, the spiral inductor is extensively used in hybrid and monolithic microwave integrated circuits (MICs). In particular, the compact size and low cost circuits used in wireless applications in the L-band and S-band are based on such inductors as matching elements.

In addition, because of the rapidly growing use of MICs in radar satellite and mobile communications electronic warfare (EW) and missiles, couplers and filter technology have undergone substantial change in terms of bandwidth size and cost. For example, in

wireless applications, a 90-degree hybrid-coupler is needed to determine the phase error of the transmitter using $\pi/4$ quadrature phase-shift keying (QPSK) modulation scheme-common to digital cellular radio systems. Basic requirements for this coupler are small size, low cost and tight amplitude balance, and quadrature phase between the output ports. These were met by coupled-line couplers using the meander line approach [11–13] and spiral configuration [13] on high-dielectric constant compatible with MICs and meander configuration [11] on a GaAs substrate compatible with MMICs. Satellite airborne communications and EW systems require small size, lightweight low-cost filters. Coupled-microstrip and stripline filters are very suitable for wideband applications where the demand on selectivity is not severe. Various kinds of filters can be realized using microstrip- type structures. For wireless applications, however, miniature versions of these filters are required because of space and cost constraints. Hairpin-line and combline filters using resonators on high-dielectric constant ($\varepsilon_r = 80$ and 90) substrate or embedded in dielectric cavities have been developed and can be designed using traditional methods and/or simulators.

3. HYBRID MODE ANALYSIS OF MULTILAYER PLANAR STRUCTURES WITH UNIAXIAL ANISOTROPY IN BILATERAL CONFIGURATION

An increasing use of multilayer multiconductor planar structures in the development of many microwave devices is one of the major trends in the RF/microwave area. Layers of suitable materials may be added to improve the performances of a device or may be required as essential building in the design of a component. For example, in microstrip couplers, extra layers of dielectrics may be used to enhance the directivity [9, 14–16], whereas the structure of a finline isolator [17, 18] consists in principle of four layers of which one is ferrite. Multilayer multiconductor structures are also reported to be used in high-speed digital integrated circuits [19, 20].

The spectral domain approach (S.D.A) is a powerful tool for microwave circuit design due to its efficiency. This method solves the Maxwell's equations in the Fourier domain by expressing the EM field in discrete (continuous) spectrum for shielded (open) structures. Introduced by Itoh and Mittra [21], the S.D.A method is essentially a procedure for computing the Green's functions by fourier decomposition, reducing the problem to that of solving algebraic equations. Provided that the basis set for the moment method solution can be transformed analytically, it reduces the computation effort to

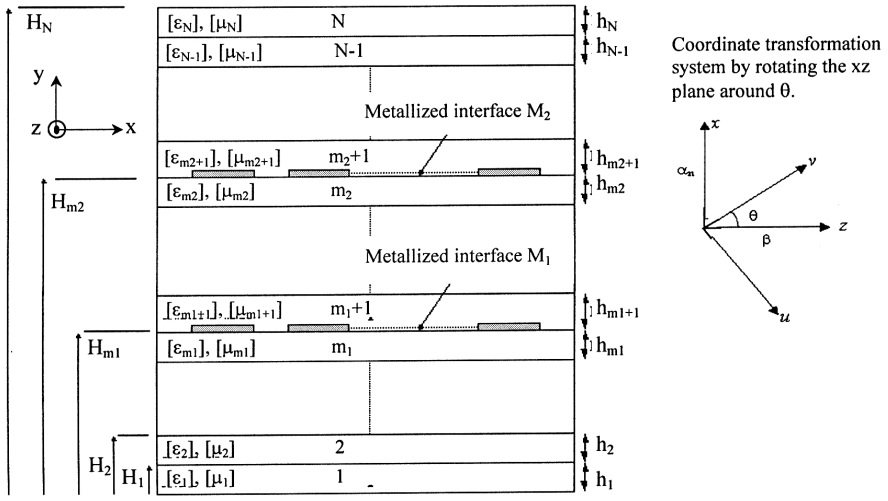

Figure 1. View of a multilayer bilateral coupled planar structure on anisotropic medium.

the evaluation of integrals or series in one or two dimensions. In SDA, Galerkin's method is used to yield a homogeneous system of equations to determine the propagation constant and the amplitude of current distributions from which the characteristic impedance is derived. In each of these methods, the fourier transform is taken along the direction parallel to the substrate and perpendicular to the strip. By virtue of the fourier transform domain analysis and Galerkin's method, S.D.A has several features: easy formulation in the form of pairs of algebra equations, variational nature in determination of the propagation constant, identification of the physical nature of the mode for each solution corresponding to the basis functions.

The S.D.A was applied to the analysis of the mixed coupling in bilateral multilayer microwave circuits printed on uniaxial anisotropic substrates (Fig. 1). In Figure 2, some examples of these coupled structures are shown.

In order to generalize the dyadic Green's function of these structures, the spectral domain immittance approach [6] was extended to anisotropic multilayer structures. In this approach, the field formulation for β calculation is bypassed and a direct formulation of the eigenvalue equation is possible without knowledge of the field coefficients. This technique makes use of a coordinate transformation as shown in Fig. 1. All the field components are a superposition of

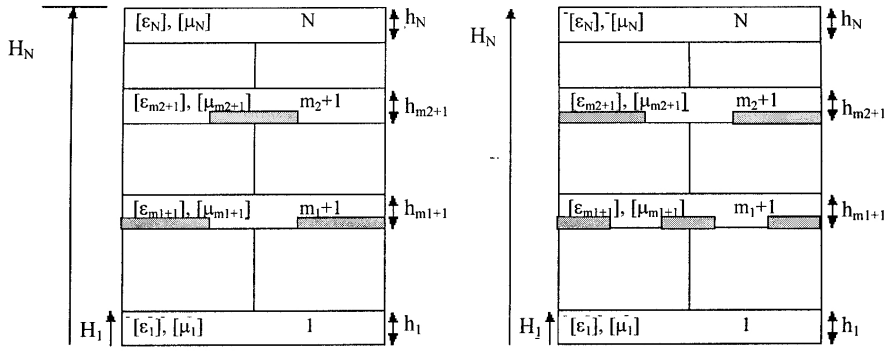

Figure 2. Multilayered bilateral coupled planar structures.

inhomogeneous (in y) plane waves that are propagating in the direction θ of the z-axis, with $\theta = \cos^{-1}(\beta/\delta)$ where $\delta = \sqrt{\alpha_n^2 + \beta^2}$. α_n and β are respectively the spectral parameter and the phase constant. For each θ hybrid waves may be decomposed into LSM ($H_y = 0$) and LSE ($E_y = 0$) in the (v, y, u) coordinate system.

The tangential components of the EM field are expressed in a dielectric layer i ($i = 1 \ldots N$) from Maxwell's equations versus E_y and H_y as:

$$\tilde{E}_x = -j\alpha_n \frac{\varepsilon_y}{\varepsilon_c\,(\alpha_n^2 + \beta^2)} \frac{\partial \tilde{E}_y}{\partial y} + \beta \frac{\omega \mu_y}{(\alpha_n^2 + \beta^2)} \tilde{H}_y \tag{1a}$$

$$\tilde{E}_z = -j\beta \frac{\varepsilon_y}{\varepsilon_c\,(\alpha_n^2 + \beta^2)} \frac{\partial \tilde{E}_y}{\partial y} - \alpha_n \frac{\omega \mu_y}{(\alpha_n^2 + \beta^2)} \tilde{H}_y \tag{1b}$$

$$\tilde{H}_x = -\beta \frac{\omega \varepsilon_y}{(\alpha_n^2 + \beta^2)} \tilde{E}_y - j\alpha_n \frac{\mu_y}{\mu_c\,(\alpha_n^2 + \beta^2)} \frac{\partial \tilde{H}_y}{\partial y} \tag{1c}$$

$$\tilde{H}_z = \alpha_n \frac{\omega \varepsilon_y}{(\alpha_n^2 + \beta^2)} \tilde{E}_y - j\beta \frac{\mu_y}{\mu_c\,(\alpha_n^2 + \beta^2)} \frac{\partial \tilde{H}_y}{\partial y} \tag{1d}$$

The index $\sim$ represents the Fourier transform following x. And $\varepsilon_c = \varepsilon_x = \varepsilon_z,\ \mu_c = \mu_x = \mu_z$.

The EM field components are then evaluated in the new coordinate system (v, y, u) via relations .

$$\begin{bmatrix} \tilde{c}_u \\ \tilde{c}_v \end{bmatrix} = \begin{bmatrix} -\cos\theta & \sin\theta \\ \sin\theta & \cos\theta \end{bmatrix} \begin{bmatrix} \tilde{c}_x \\ \tilde{c}_z \end{bmatrix} \text{ (where } c = E \text{ or } H) \tag{2}$$

where: $\sin\theta = \alpha_n/\delta$ and $\cos\theta = \beta/\delta$ with $\delta = \sqrt{\alpha_n^2 + \beta^2}$.

The normal EM field components must satisfy to the following wave equations in an anisotropic dielectric layer i ($i = 1 \ldots N$):

For modes L.S.E modes:

$$\frac{\partial^2 \tilde{H}_y}{\partial y^2} + \frac{\mu_c}{\mu_y}\left(\omega^2 \varepsilon_c \mu_y - \alpha_n^2 - \beta^2\right)\tilde{H}_y = 0 \tag{3}$$

with: $\gamma_i^{\mathrm{LSE}} = \sqrt{\frac{\mu_c}{\mu_y}\left(\alpha_n^2 + \beta^2 - \omega^2 \varepsilon_c \mu_y\right)}$ and for L.S.M modes:

$$\frac{\partial^2 \tilde{E}_y}{\partial y^2} + \frac{\varepsilon_c}{\varepsilon_y}\left(\omega^2 \varepsilon_y \mu_c - \alpha_n^2 - \beta^2\right)\tilde{E}_y = 0 \tag{4}$$

with: $\gamma_i^{\mathrm{LSM}} = \sqrt{\frac{\varepsilon_c}{\varepsilon_y}\left(\alpha_n^2 + \beta^2 - \omega^2 \varepsilon_y \mu_c\right)}$. The solutions of (3) and (4) are given by:

For $i \leq m$:

$$\tilde{H}_{yi}(\alpha_n, y) = C_i \sinh\left(\gamma_i^{\mathrm{LSE}}(y - H_i)\right) + D_i \cosh\left(\gamma_i^{\mathrm{LSE}}(y - H_i)\right) \tag{5a}$$

$$\tilde{E}_{yi}(\alpha_n, y) = A_i \sinh\left(\gamma_i^{\mathrm{LSM}}(y - H_i)\right) + B_i \cosh\left(\gamma_i^{\mathrm{LSM}}(y - H_i)\right) \tag{5b}$$

For $i \geq m + 1$:

$$\tilde{H}_{yi}(\alpha_n, y) = C_i \sinh\left(\gamma_i^{\mathrm{LSE}}(H_i - y)\right) + D_i \cosh\left(\gamma_i^{\mathrm{LSE}}(H_i - y)\right) \tag{6a}$$

$$\tilde{E}_{yi}(\alpha_n, y) = A_i \sinh\left(\gamma_i^{\mathrm{LSM}}(H_i - y)\right) + B_i \cosh\left(\gamma_i^{\mathrm{LSM}}(H_i - y)\right) \tag{6b}$$

where $m = (m_1 \text{ or } m_2)$ and $H_i = \sum_1^i h_i$.

3.1. Evaluation of Dyadic Green's Functions

The edge-coupled planar structures can, in certain specific applications, being replaced by bilateral coupled structures because of the flexibility offered by this configuration in the design of the filters and directional couplers. The analysis of this structure consists initially in the determination of Green's functions by the immittance approach technique extended to multilayered configurations. For that purpose, one establishes the equivalent circuits of the modes LSE ($E_y = 0$) and LSM ($H_y = 0$). The equivalent circuits of the two-coupled structures Microstrip/Slotline and CPW/Slotline are represented in Figs. 3 and 4 respectively:

In these circuits, (J_u, J_v) represent the current sources of LSE and LSM modes respectively and (E_u, E_v) the electric sources of LSE and

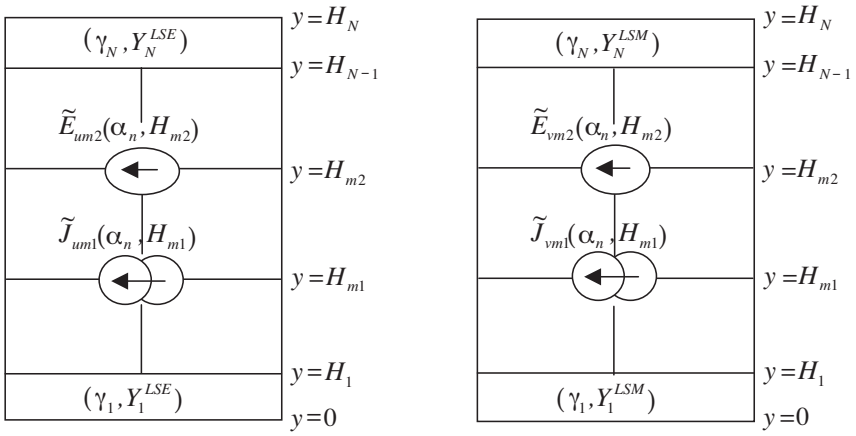

Figure 3. Equivalent circuit for a microstrip/slotline structure for LSE/LSM modes respectively.

LSM modes respectively. These sources exist on the two metallized interfaces M_1 and/or M_2. The equivalent circuits being established, one will now calculate the dyadic Green's functions following the nature of metallization existing on the two-metallized interfaces. To this end, one must calculate these functions in the reference (v, y, u) knowing that it is always possible to come back to the initial reference mark (x, y, z) via (2).

The impedance form of dyadic Green's functions, which relies the tangential components of the electric field to those of the current on the two metallized interfaces, is given as

$$\begin{pmatrix} \tilde{E}_{um1}(\alpha_n, H_{m1}) \\ \tilde{E}_{vm1}(\alpha_n, H_{m1}) \\ \tilde{E}_{um2}(\alpha_n, H_{m2}) \\ \tilde{E}_{vm2}(\alpha_n, H_{m2}) \end{pmatrix} = \begin{bmatrix} Z_{11}^h & 0 & Z_{12}^h & 0 \\ 0 & Z_{11}^e & 0 & Z_{12}^e \\ Z_{21}^h & 0 & Z_{22}^h & 0 \\ 0 & Z_{21}^e & 0 & Z_{22}^e \end{bmatrix} \begin{pmatrix} \tilde{J}_{um1}(\alpha_n) \\ \tilde{J}_{vm1}(\alpha_n) \\ \tilde{J}_{um2}(\alpha_n) \\ \tilde{J}_{vm2}(\alpha_n) \end{pmatrix} \quad (7)$$

The parameters Z_{ij}^h or Z_{ij}^e concern the LSE and LSM modes respectively, where i and j indicate the interfaces containing the metallization ($i, j = m_1$ or m_2). The Z_{ij} parameters (with $i \neq j$) can be interpreted as the transfer impedances expressing the contribution of source at $y = i$ to the field at $y = j$.

The next step will be to calculate the elements of matrix Z by applying the theorem of superposition.

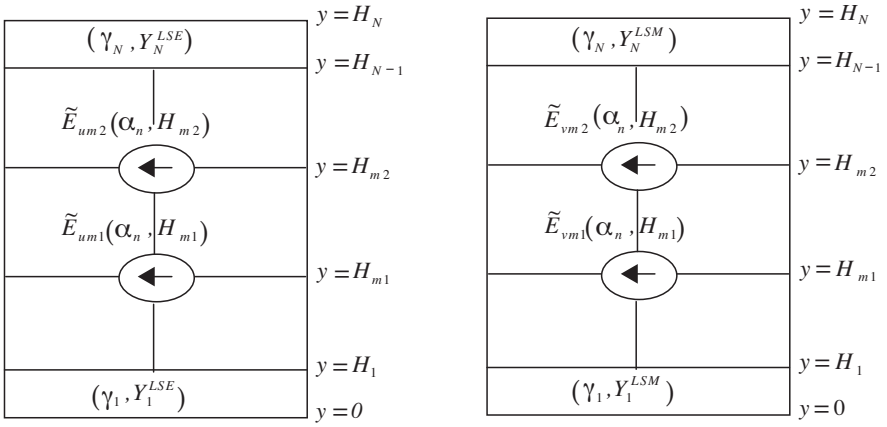

Figure 4. Equivalent circuit for a CPW/slotline structure for LSE/LSM modes respectively.

3.2. Calculation of the Elements of the Impedance Green's Matrix

3.2.1. Case of the LSE Modes

For this mode, the goal is to determine the elements of Green's matrix impedance according to the following system

$$\begin{pmatrix} \tilde{E}_{um1}(\alpha_n, H_{m1}) \\ \tilde{E}_{um2}(\alpha_n, H_{m2}) \end{pmatrix} = \begin{bmatrix} Z_{11}^h & Z_{12}^h \\ Z_{21}^h & Z_{22}^h \end{bmatrix} \cdot \begin{pmatrix} \tilde{J}_{um1}(\alpha_n) \\ \tilde{J}_{um2}(\alpha_n) \end{pmatrix} \tag{8}$$

The impedances parameters Z_{22}^h and Z_{12}^h are determined in absence of metallization at $y = H_{m1}$ ($J_{um1} = 0$). The obtained configuration is that of a multilayer planar structure with one metallized plane located at $y = H_{m2}$.

The impedances parameters Z_{11}^h and Z_{21}^h are determined in absence of metallization at $y = H_{m2}$ ($J_{um2} = 0$). The obtained configuration is that of a multilayer planar structure with one metallized plane located at $y = H_{m1}$.

3.2.1.1. Calculation of the self-impedances for each metallized interface Z_{22}^h and Z_{11}^h

The impedances Z_{11}^h and Z_{22}^h are respectively defined by the

following expressions:

$$Z_{11}^h = \left.\frac{\tilde{E}_{um1}(\alpha_n, H_{m1})}{\tilde{J}_{um1}}\right|_{\tilde{J}_{um2}=0} \tag{9}$$

$$Z_{22}^h = \left.\frac{\tilde{E}_{um2}(\alpha_n, H_{m2})}{\tilde{J}_{um2}}\right|_{\tilde{J}_{um1}=0} \tag{10}$$

The mode of calculation of the two latter parameters is identical to that developed for multilayer configuration with one metallization plane [14]. It is about determining the impedances seen at $y = H_{m1}$ (in absence of M_2) or at $y = H_{m2}$ (in absence of M_1), these impedances are indicated by Z_{11}^h and Z_{22}^h respectively.

The application of the boundary conditions for the tangential components of electric fields on the two metallized interfaces M_1 and M_2, leads to the expressions of Z_{11}^h and Z_{22}^h [22].

3.2.1.2. Determination of the transfer impedances Z_{12}^h and Z_{21}^h

The transfer impedance parameter Z_{12}^h is defined by the following formula

$$Z_{12}^h = \left.\frac{\tilde{E}_{um1}(\alpha_n, H_{m1})}{\tilde{J}_{um2}}\right|_{\tilde{J}_{um1}=0} \tag{11}$$

which can be also written as

$$\begin{aligned} Z_{12}^h = & \frac{\tilde{E}_{um1}(\alpha_n, H_{m1})}{\tilde{E}_{u(m1+1)}(\alpha_n, H_{m1+1})} \frac{\tilde{E}_{u(m1+1)}(\alpha_n, H_{m1+1})}{\tilde{E}_{u(m1+2)}(\alpha_n, H_{m1+2})} \\ & \cdots \frac{\tilde{E}_{u(m2-1)}(\alpha_n, H_{m2-1})}{\tilde{E}_{um2}(\alpha_n, H_{m2})} \frac{\tilde{E}_{um2}(\alpha_n, H_{m2})}{\tilde{J}_{um2}} \end{aligned} \tag{12}$$

According to the continuity relations applied to the various interfaces of the structure, we have

$$\begin{array}{rlcl} \text{at} \quad y = H_{m1} & : & \tilde{E}_{um1}(\alpha_n, H_{m1}) & = \tilde{E}_{u(m1+1)}(\alpha_n, H_{m1}) \\ y = H_{m1+1} & : & \tilde{E}_{u(m1+1)}(\alpha_n, H_{m1+1}) & = \tilde{E}_{u(m1+2)}(\alpha_n, H_{m1+1}) \\ \vdots & & \vdots & \vdots \\ y = H_{m2-1} & : & \tilde{E}_{u(m2-1)}(\alpha_n, H_{m2-1}) & = \tilde{E}_{um2}(\alpha_n, H_{m2-1}) \end{array}$$

Equation (12) can then be reformulated as

$$Z_{12}^h = \frac{\tilde{E}_{u(m1+1)}(\alpha_n, H_{m1})}{\tilde{E}_{u(m1+1)}(\alpha_n, H_{m1+1})} \frac{\tilde{E}_{u(m1+2)}(\alpha_n, H_{m1+1})}{\tilde{E}_{u(m1+2)}(\alpha_n, H_{m1+2})}$$

$$\cdots \frac{\tilde{E}_{um2}(\alpha_n, H_{m2-1})}{\tilde{E}_{um2}(\alpha_n, H_{m2})} \frac{\tilde{E}_{um2}(\alpha_n, H_{m2})}{\tilde{J}_{um2}} \tag{13}$$

In other hand, $\tilde{E}_{ui}(\alpha_n, y)$ is given according to (2) and (5a) as:

$$\tilde{E}_{ui}(\alpha_n, y) = -\frac{\omega\mu_{yi}}{\rho}\left\{C_i \sinh\left(\gamma_i^{\mathrm{LSE}}(y - H_{i-1})\right) + D_i \cosh\left(\gamma_i^{\mathrm{LSE}}(y - H_{i-1})\right)\right\} \tag{14}$$

which implies that

$$\begin{aligned} \frac{\tilde{E}_{ui}(\alpha_n, H_{i-1})}{\tilde{E}_{ui}(\alpha_n, H_i)} &= \frac{D_i}{C_i \sinh\left(\gamma_i^{\mathrm{LSE}} h_i\right) + D_i \cosh\left(\gamma_i^{\mathrm{LSE}} h_i\right)} \\ &= \frac{1}{\left(\dfrac{C_i}{D_i} + \coth\left(\gamma_i^{\mathrm{LSE}} h_i\right)\right) \sinh\left(\gamma_i^{\mathrm{LSE}} h_i\right)} \end{aligned} \tag{15}$$

with

$$\frac{C_i}{D_i} = \frac{Y_{i-1}^h}{Y_i^{\mathrm{LSE}}}$$

where

$$Y_i^{\mathrm{LSE}} = -\frac{\tilde{H}_{vi}}{\tilde{E}_{ui}} = \frac{\gamma_i^{\mathrm{LSE}}}{j\omega\mu_{ci}}$$

which gives

$$\frac{\tilde{E}_{ui}(\alpha_n, H_{i-1})}{\tilde{E}_{ui}(\alpha_n, H_i)} = \frac{Y_i^{\mathrm{LSE}}}{\left(Y_i^{\mathrm{LSE}} \coth\left(\gamma_i^{\mathrm{LSE}} h_i\right) + Y_{(i-1)-}^h\right) \sinh\left(\gamma_i^{\mathrm{LSE}} h_i\right)} \tag{16}$$

Then, from (13), one deduces the following relation

$$Z_{12}^h = \prod_{i=m1+1}^{m2} \frac{\tilde{E}_{ui}(\alpha_n, H_{i-1})}{\tilde{E}_{ui}(\alpha_n, H_i)} \cdot Z_{22}^h \tag{17}$$

Finally, when associating (16) with (17), one obtains

$$Z_{12}^h = \prod_{i=m1+1}^{m2} \frac{Y_i^{\mathrm{LSE}}}{\left(Y_i^{\mathrm{LSE}} \coth\left(\gamma_i^{\mathrm{LSE}} h_i\right) + Y_{(i-1)-}^h\right) \sinh\left(\gamma_i^{\mathrm{LSE}} h_i\right)} \cdot Z_{22}^h \tag{18}$$

The other transfer impedance Z_{21}^h is defined by the following formula

$$Z_{21}^h = \left.\frac{\tilde{E}_{um2}(\alpha_n, H_{m2})}{\tilde{J}_{um1}}\right|_{\tilde{J}_{um2}=0} \tag{19}$$

which can be written as

$$Z_{21}^{h} = \frac{\tilde{E}_{um2}(\alpha_n, H_{m2})}{\tilde{E}_{u(m2-1)}(\alpha_n, H_{m2-1})} \frac{\tilde{E}_{u(m2-1)}(\alpha_n, H_{m2-1})}{\tilde{E}_{u(m2-2)}(\alpha_n, H_{m2-2})} \cdots \frac{\tilde{E}_{u(m1+1)}(\alpha_n, H_{m1+1})}{\tilde{E}_{um1}(\alpha_n, H_{m1})} \frac{\tilde{E}_{um1}(\alpha_n, H_{m1})}{\tilde{J}_{um1}} \tag{20}$$

According to the continuity relations applied to the different planes of the structure, one knows that

$$\begin{array}{lcccc} \text{at} & y = H_{m2-1} & : & \tilde{E}_{u(m2-1)}(\alpha_n, H_{m2-1}) & = \tilde{E}_{um2}(\alpha_n, H_{m2-1}) \\ & y = H_{m2-2} & : & \tilde{E}_{u(m2-2)}(\alpha_n, H_{m2-2}) & = \tilde{E}_{u(m2-1)}(\alpha_n, H_{m2-2}) \\ & \vdots & & \vdots & \vdots \\ & y = H_{m1} & : & \tilde{E}_{um1}(\alpha_n, H_{m1}) & = \tilde{E}_{u(m1+1)}(\alpha_n, H_{m1}) \end{array}$$

Thus, equation (20) becomes

$$Z_{21}^{h} = \frac{\tilde{E}_{um2}(\alpha_n, H_{m2})}{\tilde{E}_{um2}(\alpha_n, H_{m2-1})} \frac{\tilde{E}_{u(m2-1)}(\alpha_n, H_{m2-1})}{\tilde{E}_{u(m2-1)}(\alpha_n, H_{m2-2})} \cdots \frac{\tilde{E}_{u(m1+1)}(\alpha_n, H_{m1+1})}{\tilde{E}_{u(m1+1)}(\alpha_n, H_{m1})} \frac{\tilde{E}_{um1}(\alpha_n, H_{m1})}{\tilde{J}_{um1}} \tag{21}$$

The expression of $\tilde{E}_{ui}(\alpha_n, y)$ for ith layer is given according to (2) and (6a) as

$$\tilde{E}_{ui}(\alpha_n, y) = -\frac{\omega \mu_{yi}}{\rho} \left\{ C_i \sinh\left(\gamma_i^{\mathrm{LSE}}(H_i - y)\right) + D_i \cosh\left(\gamma_i^{\mathrm{LSE}}(H_i - y)\right) \right\} \tag{22}$$

which implies that

$$\begin{aligned} \frac{\tilde{E}_{ui}(\alpha_n, H_i)}{\tilde{E}_{ui}(\alpha_n, H_{i-1})} &= \frac{D_i}{C_i \sinh\left(\gamma_i^{\mathrm{LSE}} h_i\right) + D_i \cosh\left(\gamma_i^{\mathrm{LSE}} h_i\right)} \\ &= \frac{1}{\left(\dfrac{C_i}{D_i} + \coth\left(\gamma_i^{\mathrm{LSE}} h_i\right)\right) \sinh\left(\gamma_i^{\mathrm{LSE}} h_i\right)} \end{aligned} \tag{23}$$

with

$$\frac{C_i}{D_i} = \frac{Y_{i+1}^{h}}{Y_i^{\mathrm{LSE}}}$$

which gives

$$\frac{\tilde{E}_{ui}(\alpha_n, H_i)}{\tilde{E}_{ui}(\alpha_n, H_{i-1})} = \frac{Y_i^{\mathrm{LSE}}}{\left(Y_i^{\mathrm{LSE}}\coth\left(\gamma_i^{\mathrm{LSE}}h_i\right) + Y_{(i+1)+}^{h}\right)\sinh\left(\gamma_i^{\mathrm{LSE}}h_i\right)} \quad (24)$$

Then, from (21), one deduces the following relation

$$Z_{21}^{h} = \prod_{i=m2}^{m1+1} \frac{\tilde{E}_{ui}(\alpha_n, H_i)}{\tilde{E}_{ui}(\alpha_n, H_{i-1})} \cdot Z_{11}^{h} \quad (25)$$

Finally, when associating finally the relations (24) and (25), one obtains the formula for Z_{21}^{h}

$$Z_{21}^{h} = \prod_{i=m2}^{m1+1} \frac{Y_i^{\mathrm{LSE}}}{\left(Y_i^{\mathrm{LSE}}\coth(\gamma_i h_i) + Y_{(i+1)+}^{h}\right)\sinh(\gamma_i h_i)} \cdot Z_{11}^{h} \quad (26)$$

3.2.2. Case of LSM Modes

For this mode, we must determine the elements of Green's matrix impedance according to the following system

$$\begin{pmatrix} \tilde{E}_{vm1}(\alpha_n, H_{m1}) \\ \tilde{E}_{vm2}(\alpha_n, H_{m2}) \end{pmatrix} = \begin{bmatrix} Z_{11}^{e} & Z_{12}^{e} \\ Z_{21}^{e} & Z_{22}^{e} \end{bmatrix} \cdot \begin{pmatrix} \tilde{J}_{vm1}(\alpha_n) \\ \tilde{J}_{vm2}(\alpha_n) \end{pmatrix} \quad (27)$$

While following the same steps for those previously developed for the LSE modes, we obtain the following expressions of the impedances Z_{12}^{e}, and Z_{21}^{e} for LSM modes.

$$Z_{12}^{e} = \prod_{i=m1+1}^{m2} \frac{Y_i^{\mathrm{LSM}}}{\left(Y_i^{\mathrm{LSM}}\coth(\gamma_i h_i) + Y_{(i-1)-}^{e}\right)\sinh(\gamma_i h_i)} \cdot Z_{22}^{e} \quad (28)$$

$$Z_{21}^{e} = \prod_{i=m2}^{m1+1} \frac{Y_i^{\mathrm{LSM}}}{\left(Y_i^{\mathrm{LSM}}\coth(\gamma_i h_i) + Y_{(i+1)+}^{e}\right)\sinh(\gamma_i h_i)} \cdot Z_{11}^{e} \quad (29)$$

with

$$Y_i^{\mathrm{LSM}} = \frac{\tilde{H}_{ui}}{\tilde{E}_{vi}} = \frac{j\omega\varepsilon_{ci}}{\gamma_i^{\mathrm{LSM}}}$$

Z_{11}^{e} and Z_{22}^{e} are the LSM impedance parameters seen at $y = H_{m1}$ (in absence of M_2) and at $y = H_{m2}$ (in absence of M_1), respectively. The application of the boundary conditions for the tangential components

of electric fields on the two metallized interfaces M_1 or M_2, leads to the expressions of Z^e_{11} and Z^e_{22} [22].

Having calculated all the elements of the Green's matrix impedance, we return to the (x, y, z) reference via (2) which gives:

$$\begin{pmatrix} \tilde{E}_{xm1}(\alpha_n, H_{m1}) \\ \tilde{E}_{zm1}(\alpha_n, H_{m1}) \\ \tilde{E}_{xm2}(\alpha_n, H_{m2}) \\ \tilde{E}_{zm2}(\alpha_n, H_{m2}) \end{pmatrix} = \begin{bmatrix} G_{11} & G_{12} & G_{13} & G_{14} \\ G_{21} & G_{22} & G_{23} & G_{24} \\ G_{31} & G_{32} & G_{33} & G_{34} \\ G_{41} & G_{42} & G_{43} & G_{44} \end{bmatrix} \begin{pmatrix} \tilde{J}_{xm1}(\alpha_n) \\ \tilde{J}_{zm1}(\alpha_n) \\ \tilde{J}_{xm2}(\alpha_n) \\ \tilde{J}_{zm2}(\alpha_n) \end{pmatrix} \tag{30}$$

with:

$$\begin{aligned} G_{11} &= Z^h_{11}\cos^2\theta + Z^e_{11}\sin^2\theta; & G_{12} &= \left[Z^e_{11} - Z^h_{11}\right]\sin\theta\cos\theta \\ G_{13} &= Z^h_{12}\cos^2\theta + Z^e_{12}\sin^2\theta; & G_{14} &= \left[Z^e_{12} - Z^h_{12}\right]\sin\theta\cos\theta \\ G_{21} &= G_{12}; & G_{22} &= Z^e_{11}\cos^2\theta + Z^h_{11}\sin^2\theta \\ G_{23} &= G_{14}; & G_{24} &= Z^e_{12}\cos^2\theta + Z^h_{12}\sin^2\theta \end{aligned}$$

$$\begin{aligned} G_{31} &= Z^h_{21}\cos^2\theta + Z^e_{21}\sin^2\theta; & G_{32} &= \left[Z^e_{21} - Z^h_{21}\right]\sin\theta\cos\theta \\ G_{33} &= Z^h_{22}\cos^2\theta + Z^e_{22}\sin^2\theta; & G_{34} &= \left[Z^e_{22} - Z^h_{22}\right]\sin\theta\cos\theta \\ G_{41} &= G_{32}; & G_{42} &= Z^e_{21}\cos^2\theta + Z^h_{21}\sin^2\theta \\ G_{43} &= G_{34}; & G_{44} &= Z^e_{22}\cos^2\theta + Z^h_{22}\sin^2\theta \end{aligned}$$

where $G_{i,j}$ represent the elements of dyadic Green's matrix $[G]$. As shown through (30) when dealing with a general multilayer multiconductor structure, the order of the Green's function matrix depends only on the number of layers of conductors. In fact, each additional conductor layer increases the $[G]$ matrix order by two.

4. SYSTEM RESOLUTION BY GALERKIN METHOD

Let us consider the system of equations described in (30) and discuss the solution of the Green's impedances; note that the current is the only parameter to model on the two metallized interfaces M_1 and M_2 of the structure (this kind of coupling is widely used in many configurations such as microstrip/microstrip or broadside-edge coupled structures).

In order to convert (30) into a set of linear homogeneous equation we initially require defining some sets of basis functions for expanding J. The system to be solved contains eight unknown factors, namely the tangential components of the current and the electric field. However, four unknowns can be eliminated by applying the Galerkin's procedure.

With this technique, we start by expanding in the Fourier domain the current densities on M_1 (Jx_{m1}, Jz_{m1}) and M_2 (Jx_{m2} and Jz_{m2}) as functions of suitable basis functions:

$$\tilde{J}_{xm1}(\alpha_n) = \sum_{p=1}^{P} a_p \tilde{J}_{xp}(\alpha_n) \tag{31a}$$

$$\tilde{J}_{zm1}(\alpha_n) = \sum_{q=1}^{Q} b_p \tilde{J}_{zq}(\alpha_n) \tag{31b}$$

$$\tilde{J}_{xm2}(\alpha_n) = \sum_{r=1}^{R} c_r \tilde{J}_{xr}(\alpha_n) \tag{31c}$$

$$\tilde{J}_{zm2}(\alpha_n) = \sum_{s=1}^{S} d_s \tilde{J}_{zs}(\alpha_n) \tag{31d}$$

The parameters a_p, b_q, c_r, d_s are the unknown complex scalar coefficients to determine. After substituting (31) in (30) and taking the inner products with test functions $\tilde{J}x_{p'}$, $\tilde{J}z_{q'}$, $\tilde{J}x_{r'}$ and $\tilde{J}z_{s'}$ (chosen equal to the basis functions), and using the Parseval's identity, we obtain a homogenous system of algebraic equations with (P+Q+R+S) unknown coefficients a_p, b_q, c_r, and d_s:

$$\sum_{p=1}^{P} C^{11}_{xp,xp'}(\beta)a_p + \sum_{q=1}^{Q} C^{12}_{zq,xp'}(\beta)b_q + \sum_{r=1}^{R} C^{13}_{xr,xp'}(\alpha_n)c_r + \sum_{s=1}^{S} C^{14}_{zs,xp'}(\beta)d_s = 0$$

$$\sum_{p=1}^{P} C^{21}_{xp,zq'}(\beta)a_p + \sum_{q=1}^{Q} C^{22}_{zq,zq'}(\beta)b_q + \sum_{r=1}^{R} C^{23}_{xr,zq'}(\alpha_n)c_r + \sum_{s=1}^{S} C^{24}_{zs,zq'}(\beta)d_s = 0$$

$$\sum_{p=1}^{P} C^{31}_{xp,xr'}(\beta)a_p + \sum_{q=1}^{Q} C^{32}_{zq,xr'}(\beta)b_q + \sum_{r=1}^{R} C^{33}_{xr,xr'}(\alpha_n)c_r + \sum_{s=1}^{S} C^{34}_{zs,xr'}(\beta)d_s = 0$$

$$\sum_{p=1}^{P} C^{41}_{xp,zs'}(\beta)a_p + \sum_{q=1}^{Q} C^{42}_{zq,zs'}(\beta)b_q + \sum_{r=1}^{R} C^{43}_{xr,zs'}(\alpha_n)c_r + \sum_{s=1}^{S} C^{44}_{zs,zs'}(\beta)d_s = 0$$

where

$$C^{i,j}_{K,L}(\omega,\beta) = \sum_{n} G_{ij}(\alpha_n,\beta)\tilde{J}_K \tilde{J}^*_L \qquad (i,j = 1\ldots 4) \tag{32}$$

The non-trivial solutions of the latter system provide the propagation constants of the guided waves. The non-trivial solutions are obtained by setting the determinant of the system equal to zero and by evaluating the roots of the resulting characteristic equation for a given frequency

$$\det[C(\omega, \beta)] = 0 \tag{33}$$

The solution accuracy can be systematically improved by increasing the number of basis functions and by solving larger size matrix equations. However, if the first few basis functions are chosen to approximate the actual unknown current distribution reasonably well, the size of the matrix can be held small for an acceptable user defined accuracy of the solution.

5. VARIOUS CASES OF COUPLING

There are several types of coupling, which can be realized with miniaturized transmission lines. In the case of mixed coupling such as CPW/slotline and microstrip/slotline or self-coupling as for microstrip/microstrip or slotline/slotline, it is important to choose the adequate form of Green's functions: impedance, admittance or hybrid, in order to exploit efficiently the advantages the S.D.A. The nature of the metallization that exists on the interfaces (microstrip, slotline or CPW) influences both the quantity to model (field or current) and the basis functions choice. Hence, a code has been developed to treat such kinds of coupling.

5.1. Self-coupling

The equivalent circuits of LSE and LSM waves are exclusively constituted by current sources (e.g., microstrip/microstrip structure) or electric field sources (e.g., slotline/slotline or CPW/slotline). In the first case, it is more advantageous to model the current on the strips. Thus, we used the $[Z]$ impedance form of the Green's functions. However in the second case, it is preferable to model the field in the slots. Here, we used another alternative form of Green's functions, i.e., the $[Y]$ admittance form whose elements are deduced after inverting the $[Z]$ matrix.

5.2. Mixed Coupling

The coupling is realized between structures of different nature (microstrip/slotline for instance). Therefore, the equivalent circuits require the simultaneous existence of current and field sources. In

this case, the utilization of the impedance form of Green's functions (30) does not lead to an efficient solution. A more efficient solution is possible if (30) is rearranged and rewritten as follows for a microstrip/slotline structure:

$$\begin{pmatrix} \tilde{E}_{xm1}(\alpha_n, H_{m1}) \\ \tilde{E}_{zm1}(\alpha_n, H_{m1}) \\ J_{xm2}(\alpha_n, H_{m2}) \\ J_{zm2}(\alpha_n, H_{m2}) \end{pmatrix} = \begin{bmatrix} Hb_{11} & Hb_{12} & Hb_{13} & Hb_{14} \\ Hb_{21} & Hb_{22} & Hb_{23} & Hb_{24} \\ Hb_{31} & Hb_{32} & Hb_{33} & Hb_{34} \\ Hb_{41} & Hb_{42} & Hb_{43} & Hb_{44} \end{bmatrix} \begin{pmatrix} \tilde{J}_{xm1}(\alpha_n) \\ \tilde{J}_{zm1}(\alpha_n) \\ E_{xm2}(\alpha_n) \\ E_{zm2}(\alpha_n) \end{pmatrix} \tag{34}$$

Hence, we have modelled simultaneously the current (on the strips) and the fields (in the slots) by using the third alternative form of Green's functions i.e., the hybrid form $[Hb]$ whose elements can be deduced from those of the impedance form of Green's functions $[Z]$. Since in these couplers, both the slot and the strip are of small widths, the above arrangement should lead to a more economical and efficient solution than that achieved through (30).

6. BASIS FUNCTIONS CHOICE

An adequate choice of a set of basis functions allows to increase the precision, reduce CPU time and improve the conditioning of the matrix $[C(\omega, \beta)]$, which makes more efficient the resolution of the system (33). The selected basis functions for the current (field) must be non-zero on the metal strips (slots). This choice must respect the singular behaviour of the electromagnetic field in the vicinity of the edges to avoid the relative convergence and improve the conditioning of the final matrix $[C(\omega, \beta)]$. These functions must suitably model the current on the metal strips and ensure a good convergence. To achieve that, we have used the basis functions summarized in Tables 1 and 2 for different coupling configurations where 'w' and 's' are the strip and slot widths respectively. These functions were tested with respect to accuracy and convergence.

7. NUMERICAL RESULTS

In order to demonstrate the efficiency of the proposed technique, we have analyzed several types of bilateral coupled planar structures to determine the propagation constant, the effective permittivity as well as the guided wavelength. The obtained results were compared with the published results available in the literature. In what follows, we will take $\varepsilon_x = \varepsilon_z = \varepsilon_c$.

Table 1. Basis functions for microstrip and slotlines structures.

	Microstrip		Slotlines	
	J_{xp}	J_{zq}	E_{xp}	E_{zq}
Even mode	$\frac{\sin(p\pi x/w)}{\sqrt{1-(x/w)^2}}$	$\frac{\cos[(q-1)\pi x/w}{\sqrt{1-(x/w)^2}}$	/	/
Odd mode	/	/	$\frac{\cos[(p-1)\pi x/s]}{\sqrt{1-(x/s)^2}}$	$\frac{\sin(q\pi x/s)}{\sqrt{1-(x/s)^2}}$

Table 2. Basis functions for coupled-microstrip and coplanar structures.

			- 2w-s < x <−s	s < x < 2w+s
Coupled microstrip structures	Even mode	J_{xp}	$\frac{\sin[p\pi(x+w+s)/w]}{\sqrt{1-((x+w+s)/w)^2}}$	$\frac{\sin[p\pi(x-w-s)/w]}{\sqrt{1-((x-w-s)/w)^2}}$
		J_{zq}	$\frac{\cos[q\pi(x+w+s)/w]}{\sqrt{1-((x+w+s)/w)^2}}$	$\frac{\cos[q\pi(x-w-s)/w]}{\sqrt{1-((x-w-s)/w)^2}}$
	Odd mode	J_{xp}	$\frac{\sin[p\pi(x+w+s)/w]}{\sqrt{1-((x+w+s)/w)^2}}$	$-\frac{\sin[p\pi(x-w-s)/w]}{\sqrt{1-((x-w-s)/w)^2}}$
		J_{zq}	$\frac{\cos[q\pi(x+w+s)/w]}{\sqrt{1-((x+w+s)/w)^2}}$	$-\frac{\cos[q\pi(x-w-s)/w]}{\sqrt{1-((x-w-s)/w)^2}}$
			- w-2s < x <−w	w < x < w+2s
Coplanar structures	Even mode	E_{xq}	$\frac{\cos[q\pi(x+s+w)/s]}{\sqrt{1-((x+s+w)/s)^2}}$	$\frac{\cos[q\pi(x-s-w)/s]}{\sqrt{1-((x-s-w)/s)^2}}$
		E_{zp}	$\frac{\sin[p\pi(x+s+w)/s]}{\sqrt{1-((x+s+w)/s)^2}}$	$\frac{\sin[p\pi(x-s-w)/s]}{\sqrt{1-((x-s-w)/s)^2}}$
	Odd mode	E_{xq}	$\frac{\cos[q\pi(x+s+w)/s]}{\sqrt{1-((x+s+w)/s)^2}}$	$-\frac{\cos[q\pi(x-s-w)/s]}{\sqrt{1-((x-s-w)/s)^2}}$
		E_{zp}	$\frac{\sin[p\pi(x+s+w)/s]}{\sqrt{1-((x+s+w)/s)^2}}$	$-\frac{\sin[p\pi(x-s-w)/s]}{\sqrt{1-((x-s-w)/s)^2}}$

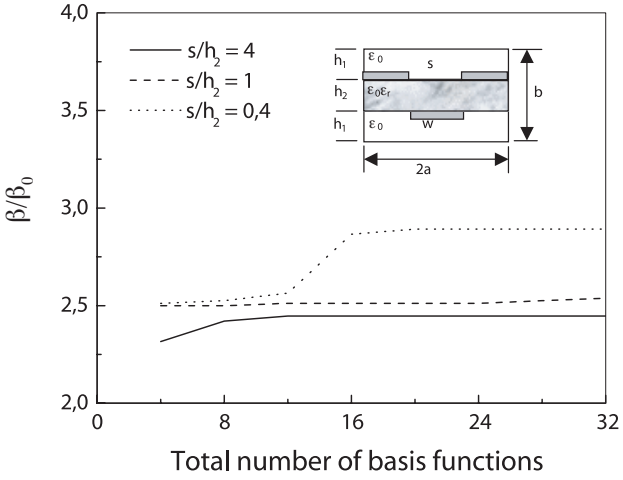

Figure 5. Convergence of the even-mode normalized phase constant versus the total number of basis functions.

7.1. Convergence

To confirm our adequate choice of basis functions, we have analysed the convergence of the normalized phase constant of a coupled microstrip/slotline structure versus the total number of basis functions $(P+Q+R+S)$ and the number of Fourier terms Ntf. The structure is printed on Epsilam-10 ($\varepsilon_c = 13$ and $\varepsilon_y = 10.3$).

The results are presented on Figures 5 and 6 for the even mode for different values of s/h_2 and on Figures 7 and 8 for the odd mode for different values of w/h_2.

Note that for the even mode, the convergence is reached for Ntf close to 120 and 16 basis functions. Beside, it is noticed that for the narrow slots ($s/h_2 < 1$), it is required necessary to increase the total number of Fourier terms in order to ensure a good convergence. In addition, it is noticed that a more significant number of Fourier terms is needed for $s/h_2 = 1$.

For the odd mode (Figs. 7 and 8), $Ntf = 100$ and 8 basis functions are enough to ensure a good convergence. In addition, these curves show clearly that a decrease of w/h_2 increases the number of Fourier terms needed to obtain the convergence. So, narrow strips for the odd mode and narrow slots for the even mode require much more Fourier terms to ensure a good convergence; this convergence being faster for the lines with large strips or slots. Note finally that the normalized phase constant decreases with the increase of the width of slot for the

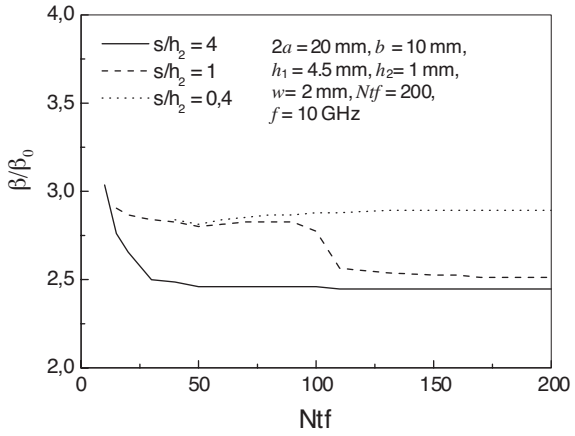

Figure 6. Convergence of the even-mode normalized phase constant versus the number of Fourier terms.

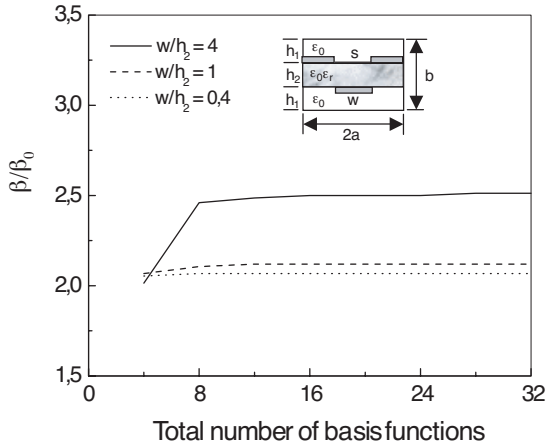

Figure 7. Convergence of the odd-mode normalized phase constant versus to the total number of basis functions.

even mode and increases with the increase of the strip width for the odd mode.

7.2. Microstrip/Coupled-microstrip

Based on our computed results, Figure 9 shows the dispersion chart of a microstrip/coupled-microstrip structure printed on sapphire substrate

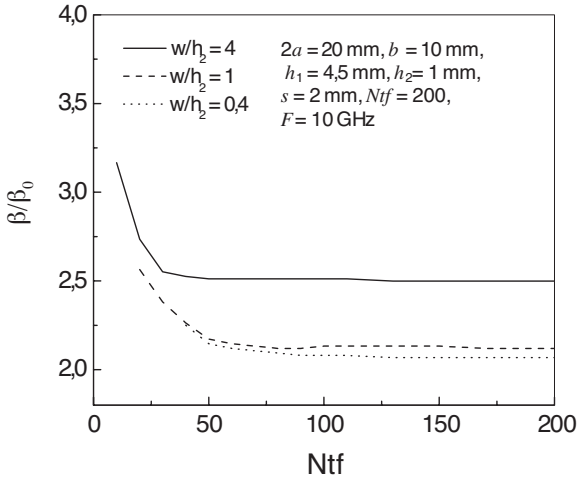

Figure 8. Convergence of the odd-mode normalized phase constant versus the number of Fourier terms.

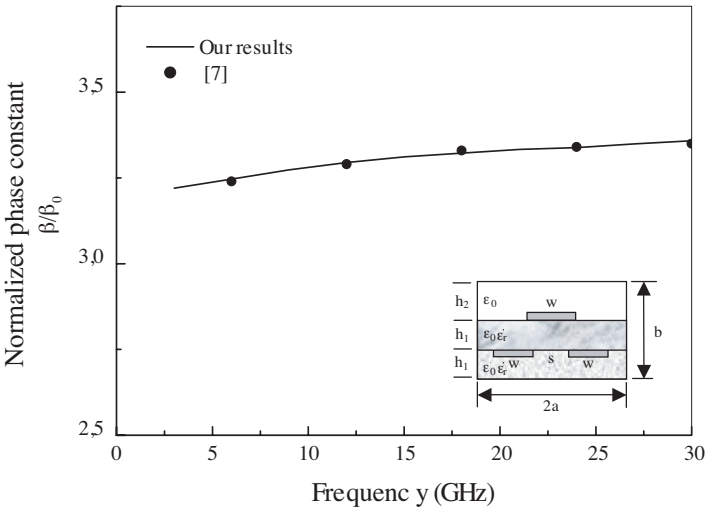

Figure 9. Dispersion chart of a microstrip/coupled-microstrip structure on sapphire substrate ($2a = 10\,\text{mm}$, $b = 6\,\text{mm}$, $h_1 = 1\,\text{mm}$, $h_2 = 4\,\text{mm}$, $w = 1\,\text{mm}$, $s = 2\,\text{mm}$).

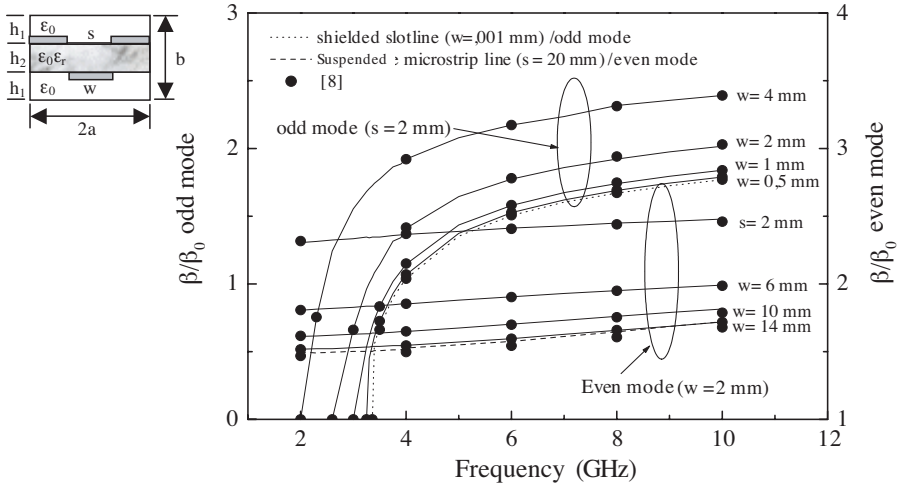

Figure 10. Normalized phase constant for microstrip/slotline structure for various widths of strip and slots on an alumina substrate ($2a = 20\,\text{mm}$, $b = 10\,\text{mm}$, $h_1 = 4.5\,\text{mm}$, $h_2 = 1\,\text{mm}$).

($\varepsilon_c = 9.4,\ \varepsilon_y = 11.6$).

Note that the variation is negligible inside the selected frequency band (3–30 GHz). The quasi-static approach would be, in this case, more adequate for the analysis of this structure. The obtained results agree well with [7] and the relative error does not exceed 0,2%.

7.3. Microstrip/slotline

Figure 10 shows the influence of the strip width variation for the even mode ("strip mode") and the slot width for the odd mode ("slot mode") for Alumina substrate ($\varepsilon_c = \varepsilon_y = 9.35$).

Note that when 'w' increases, β/β_0 of the odd mode increases contrary to the even mode where β/β_0 decrease with the increase of 's'. Note also that the increase in frequency involves the increase in β/β_0 for the two modes. For the even mode, we note a low dispersion for various values of 's' contrary to the odd mode where the variation is important. Also, note that when 'w' approaches zero for the odd mode and 's' tends to '$2a$' for the even mode, the normalized phase constant tend respectively to those of the suspended finline and a microstrip suspended line.

A control of convergence was carried out by increasing the number of spectral terms (Ntf) as well as the total number of basis functions

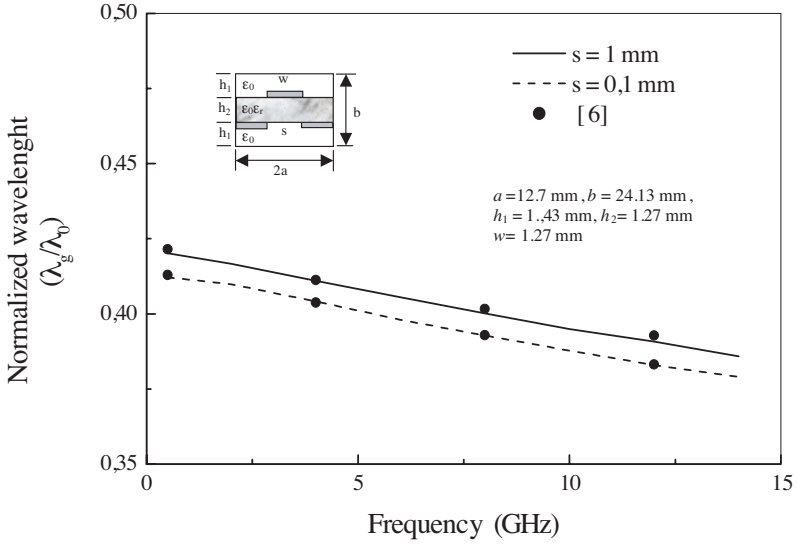

Figure 11. Dispersion characteristics of microstrip-slotline structure with $\varepsilon_c = \varepsilon_y = 8.875$.

(Nbf). The obtained results show that the convergence is ensured for $Nbf = 20$ (5 functions per component) and $Ntf = 200$. These results agree well with [8] with a relative error lower than 1%.

Figure 11 illustrates the frequency variation of the normalized wavelength (λ/λ_0) with the slot width as parameter for an isotropic substrate ($\varepsilon_c = \varepsilon_y = 8.875$). This figure shows the decreasing of the normalized wavelength versus frequency and increases when S increases. These results agree well with [6]. The relative error does not exceed 1%.

7.4. Bilateral Finline

Figure 12 shows the variation of the effective permittivity versus frequency for two different substrates. The results were compared to those published [23]. In the first case, the substrate is isotropic and non-magnetic with $\varepsilon_c = \varepsilon_y = 3.75$. The selected structure is inserted into a rectangular waveguide WR28, with $h_1 = 0.0625$ mm, $h_2 = 3.4935$ mm and $s = 0.5$ mm. In the second case, the second substrate is anisotropic with $\varepsilon_c = 3$ and $\varepsilon_y = 3.5$, with the same physical dimensions.

It is noted that the effective permittivity increases with the frequency, exhibiting a larger variation up to 30 GHz approximately.

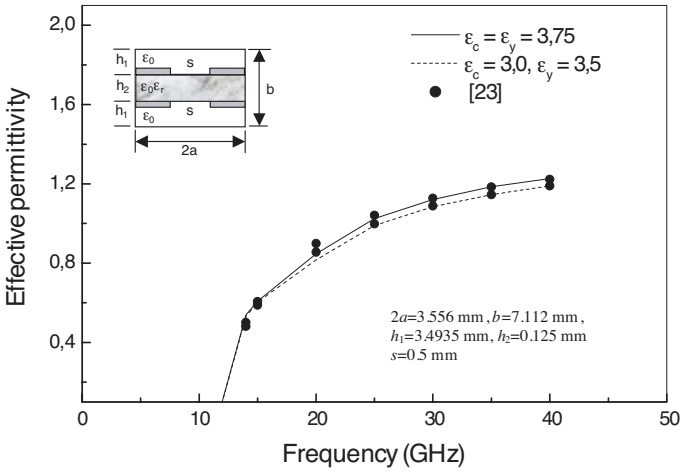

Figure 12. Effective permittivity versus frequency for a bilateral finline.

Furthermore, the two curves have the same shape and are almost identical in spite of the anisotropy of the second substrate; this is due to the low variation of the permittivity. The obtained results show good agreement with those published [23]. The relative error is lower than 1%.

To better understand the effect of the anisotropy on the effective permittivity, we have changed the dimensions to $h_1 = 0.254\,\text{mm}$, $h_2 = 3.429\,\text{mm}$ and $s = 1\,\text{mm}$ for three kinds of substrates. The results shown on Figure 13 were obtained with 5 basis functions per field component ($P = Q = R = S = 5$) and 200 Fourier terms. They agree well with [24].

Effective permittivity increases as the frequency increases. Note that the effective permittivity is of more important value for high values of the permittivity. The dispersion is accentuated for high frequencies and the anisotropy effect is amplified for the high frequencies.

7.5. Slotline/Coupled-microstrip

Figure 14 illustrates the variation of the normalized wavelength versus the slot width 's' for a bilateral slotline/coupled-microstrip-line structure printed on various types of isotropic substrates [9].

Note that the normalized wavelength increases as the slot width 's' increases and decreases with the increase of the substrate permittivity for both even and odd modes.

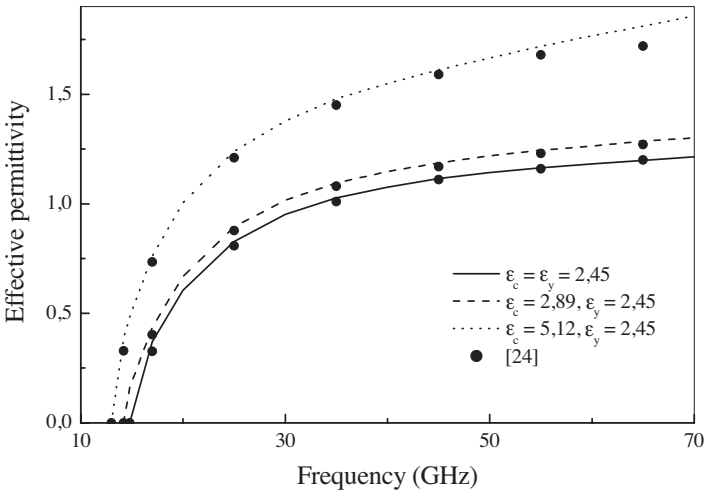

Figure 13. Effective permittivity versus frequency for a bilateral finline ($2a = 3.556\,\text{mm}$, $b = 7.112\,\text{mm}$, $h_1 = 3.429\,\text{mm}$, $h_2 = 0.254\,\text{mm}$, $s = 1\,\text{mm}$) for an isotropic substrate ($\varepsilon_c = \varepsilon_y = 2.45$) and two anisotropic substrates: PTFE cloth ($\varepsilon_c = 2.89,\ \varepsilon_y = 2.45$) and boron nitride ($\varepsilon_c = 5.12,\ \varepsilon_y = 3.4$).

In addition, the variation of normalized wavelength is more accentuated for the even mode than for the odd mode. Also, we note that for a particular value of slot width 's', the curves of the even and odd modes give the same response. This phenomenon is very useful for the design of directional couplers. Finally, it is noticed that this structure is more dispersive for substrates with high permittivity.

7.6. CPW/Slotline

We have analysed a CPW/slotline structure on RT-Duroid ($\varepsilon_c = \varepsilon_y = 2.22$). Figure 15 shows the influence of b/λ_0 and change of s'/a on the normalized wavelength for even and odd modes for two values of the slot width 's'.

We note that if the slot width 's' tends to the width of the shielding "$2a$", the normalized wavelength tend to the one of a unilateral coplanar line with three dielectric layers. Note that the observations are similar to those of Figure 15. In addition, it is noted that for a slot width $s \approx 2a$, the normalized wavelength increases with the increase of s'/a for both even and odd modes. Note the decrease in λ/λ_0 for $s'/a = 0, 15$ and for a low value of the slot width 's' for the even mode,

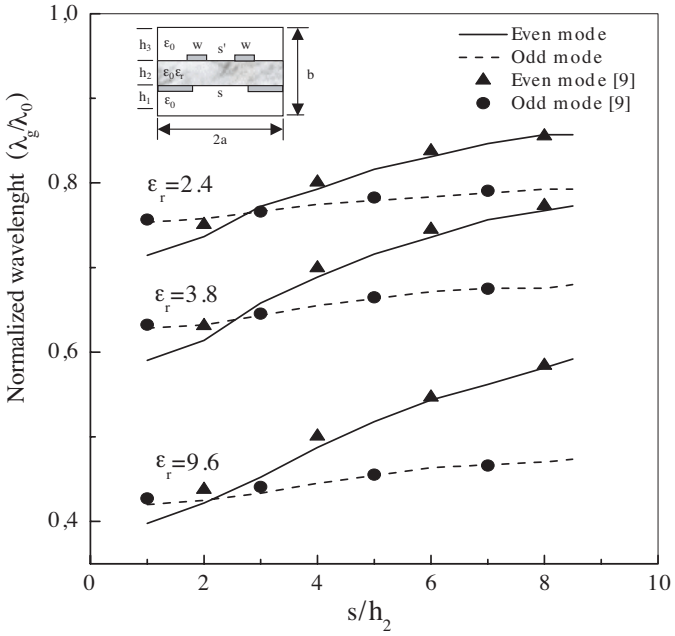

Figure 14. Normalized wavelength versus slot width 's' for a "slotline/coupled-microstrip structure ($2a = 32.8\,\text{mm}$, $b = 34.44\,\text{mm}$, $a/h_2 = h_1/h_2 = h_3/h_2 = 10$, $w/h_2 = 1.2$, $s'/2h_2 = 0.2$).

same as for values of b/λ_0 for the odd mode.

The obtained results for a slot width $s \sim 2a$ were compared to those published for a unilateral coplanar line with three layers [25]. These results show a good agreement, the relative error does not exceed 1%.

7.7. Three Line Bilateral Couplers

Three line bilateral couplers are particularly useful in communications systems to combine two signals into one without any interaction of the signal sources. Compared to the traditional coupled line design, the three-line filter has two main advantages [26]. First, the tight line spacing for designing wideband band-pass filters can be greatly relaxed, and second, the stop-band characteristics of the filter can be improved. The use of anisotropic substrate can be used to improve the coupler isolation and directivity by equalizing the coupler phase velocities. It also provides design flexibility by changing the characteristics of anisotropic materials, i.e., by varying ε_x and ε_y. In this section, we will

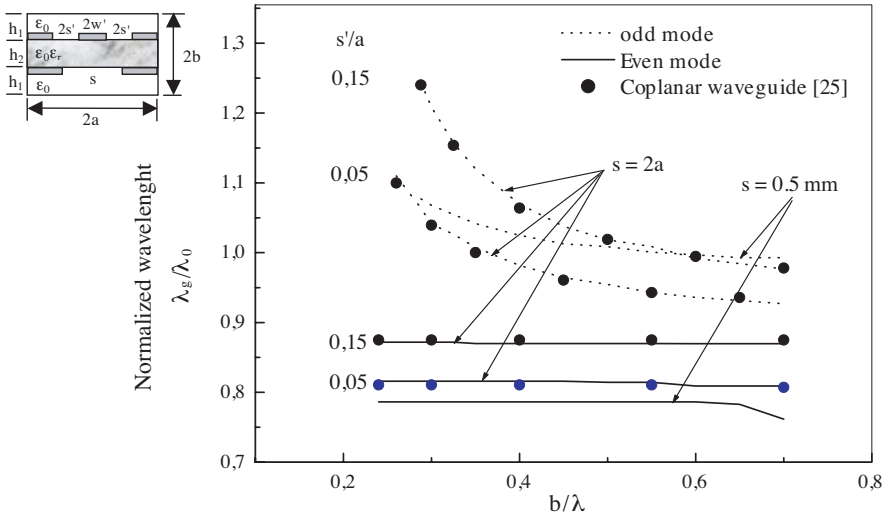

Figure 15. Normalized wavelength versus b/λ_0 for CPW/slotline structure for even and odd modes ($2a = 3.556\,\text{mm}$, $2b = 7.112\,\text{mm}$, $h_2/b = 0.03515$, $2w'/h_2 = 0.1$) on RT-Duroid ($\varepsilon_c = \varepsilon_y = 2,45$).

study two original configurations based on three line bilateral couplers, the computed results will be validated with neural network models.

7.7.1. Computed Results

Figure 16 illustrates the variation of the even-mode effective permittivity versus frequency for a three line suspended bilateral structure named three line/coupled microstrip structure printed on various types of anisotropic substrates sapphire ($\varepsilon_{c2} = 9.4$, $\varepsilon_{y2} = 11.6$), Epsilam 10 ($\varepsilon_{c2} = 13$, $\varepsilon_{y2} = 10.2$) and PTFE cloth ($\varepsilon_{c2} = 2.89$, $\varepsilon_{y2} = 2.45$). The even-mode electric field configuration in this structure is shown in Figure 17.

It is noted that the effective permittivity increases with the frequency, exhibiting a larger variation up to approximately 20 GHz. furthermore, we note that the curves for sapphire and Epsilam 10 match around 15 GHz; beyond this point the results are quite similar for the two substrates. Note also that the dispersion is accentuated for high frequencies and the anisotropy effect is amplified for the high frequencies and high values of permittivity. The results were obtained with 5 basis functions per current component ($P = Q == S = 2$) and 200 Fourier terms.

In Figure 18, we have analysed a three line bilateral coupler on

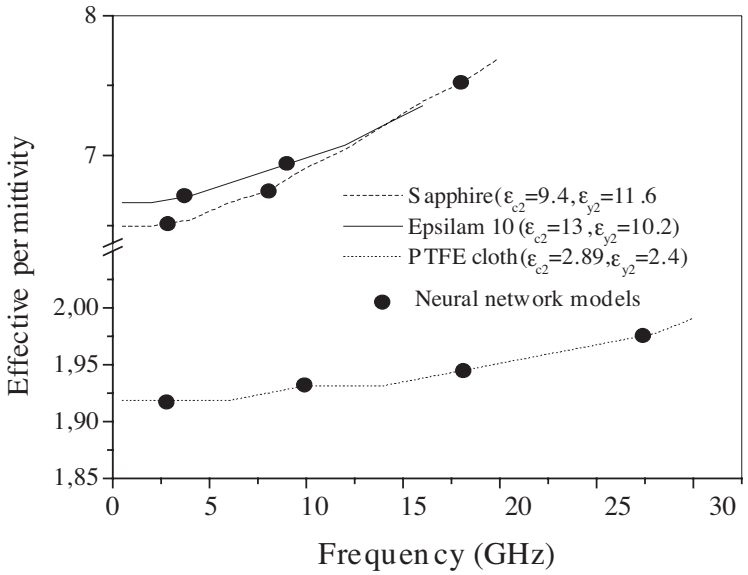

Figure 16. Comparison between obtained results and neural network models for the even-mode permittivity: case of the three line/microstrip-coupled structure printed on various anisotropic substrates with: $w_1 = 0.0125\,\text{mm}$, $s_1 = 0.5\,\text{mm}$, $w_2 = 0.05\,\text{mm}$, $s_2 = 0.5\,\text{mm}$, $2a = 3.556\,\text{mm}$, $2b = 7.112\,\text{mm}$.

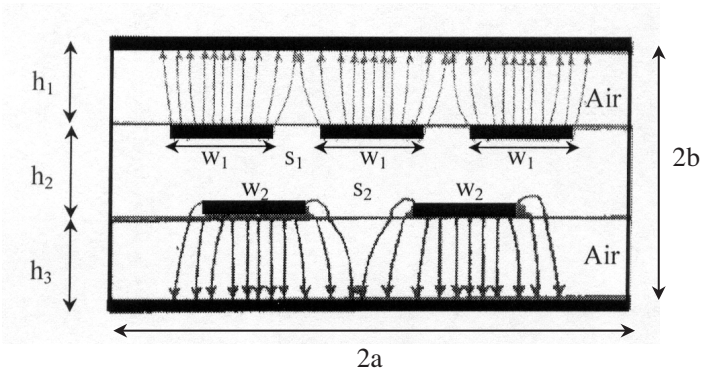

Figure 17. Electric field configuration of three line /coupled-microstrip structure for the even mode.

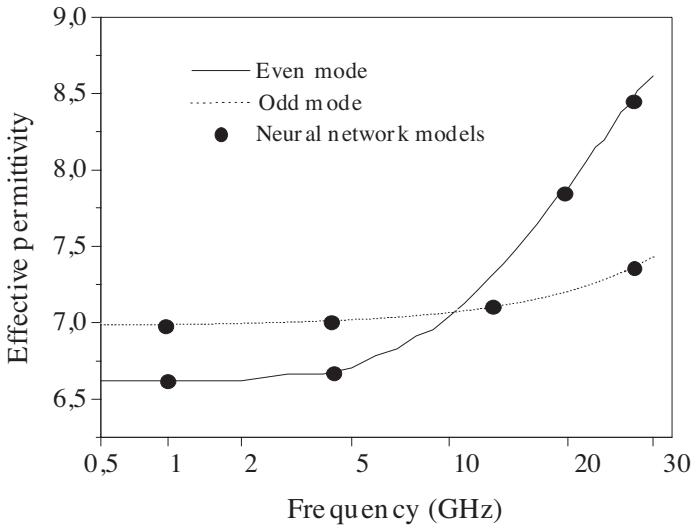

Figure 18. Comparison between obtained results and neural network models for the even- and odd-modes permittivity: case of the bilateral three-line coupler printed on sapphire with: $w_1 = 0.0125\,\text{mm}$, $s_1 = 0.5\,\text{mm}$, $2a = 3.556\,\text{mm}$, $2b = 7.112\,\text{mm}$.

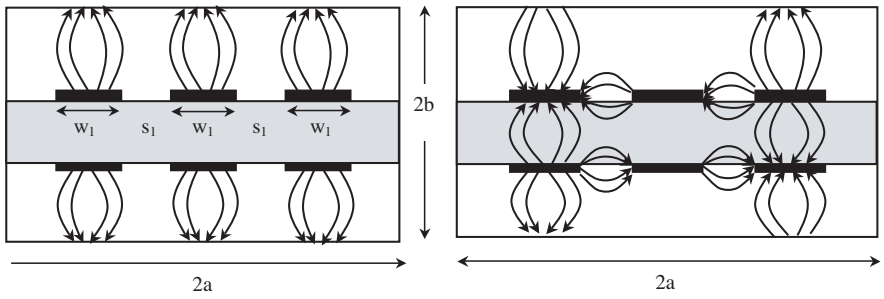

Figure 19. Electric field configuration of three line /coupled-microstrip structure for the a) even mode and b) odd-modes.

sapphire ($\varepsilon_{c2} = 9.4$, $\varepsilon_{y2} = 11.6$) for the even and odd modes. The even-mode electric field configuration in this structure is shown in Figure 19 for the odd and even modes. Note that, the variation of the effective permittivity is more accentuated for the even mode than for the odd mode.

7.7.2. Validation with Neural Networks Models

In the past few years, neural networks have been introduced as an advanced CAD tool for microwave modeling, simulation and optimization. Fast, accurate and reliable neural network models can be developed from measured or simulated microwave data. Once developed, these neural models can be used in place of computationally intensive physics/EM models of active/passive devices to speed up microwave design [27]. Neural network techniques have been used to model a wide variety of microwave devices/circuits such as transmission lines [28–31].

Neural models are much faster than original detailed physics/EM models [27, 32], more accurate than polynomial and empirical models [33], allow more dimensions than table lookup models [34] and are easier to develop when a new device/technology is introduced [27].

Furthermore, neural models have much enhanced speed/accuracy, generality, and adaptability compared to those from conventional modelling methods. In this work, we utilized these abilities of neural networks to generate neural models for effective permittivity using the neural network tool Neuromodeler [35]. NeuroModeler provides a new type of solutions for modelling problems in many engineering tasks such as electrical and physical design of circuits and systems.

The effective permittivity neural models were generated using about 300 data. The trained neural models achieve an average accuracy of 0.07%. Developed neural models were subjected to an independent test with a large set of 300 data for ε_{eff}. These data were never seen during training and the maximal test error is observed to be less than 0.03%, further confirming the reliability of our models.

Figures 16 and 17 show a comparison between computed results and the simulated ones obtained with the neural network tool Neuromodeler [35]. A very good agreement is shown.

8. CPU TIME

The CPU time is among the most important criteria to appreciate the efficiency of a numerical approach. Figures 20 and 21 show its evolution versus the number of basis functions (Nbf) and the number of spectral terms Ntf respectively for a microstrip/slotline structure on Epsilam 10 substrate ($\varepsilon_c = 13,\ \varepsilon_y = 10.3$).

Note that the CPU time increases rapidly as the number of basis functions Nb and spectral terms Ntf increases. In both cases, this increase is of exponential form. The aim here is to obtain the lowest CPU time with a good precision. This was reached with 16 basis functions and 120 Fourier terms.

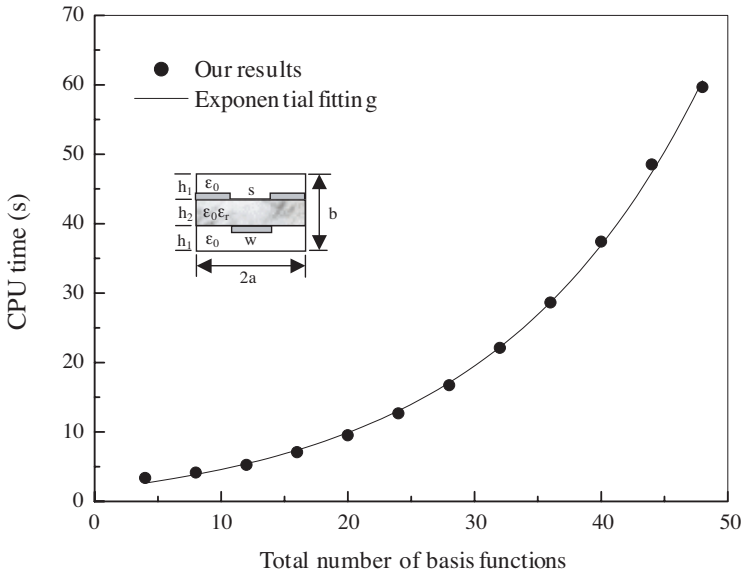

Figure 20. CPU time versus the total number of basis functions for a microstrip/slotline structure (odd mode).

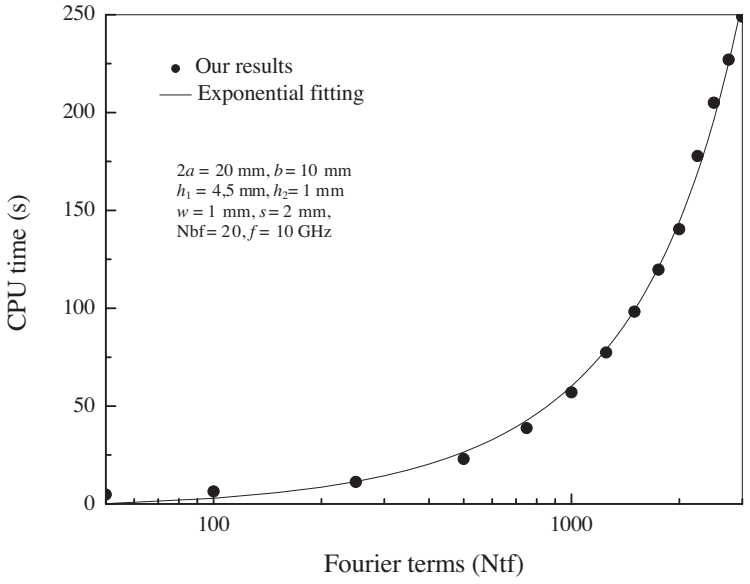

Figure 21. CPU time versus the number of Fourier terms for microstrip/slotline structure.

The results show a significant enhancement of the CPU time. In fact, our results were obtained in less than $2s$ for all tested coupled bilateral structures showing a reduction of the CPU time by a factor of 6 compared to the technique reported in [7]. In this reference, a microstrip/coupled-microstrip structure was analysed using the FDTD method.

For the slot/microstrip structure, the CPU time was divided by a factor of 2 ($P = Q = R = S = 3$) [8]. For the slot/coupled-microstrip structure [9], the CPU time is similar but we should note that the work referenced in [9] was implemented in the quasi-static mode while our proposed technique is performed in the dynamic mode. In fact, the quasi static mode does not take into account the dispersion and therefore require a shorter numerical effort than the proposed approach which is more rigorous and consider a hybrid propagation mode resulting from the superposition of LSE and LSM modes.

Furthermore, as for the CPU time, many published papers in the same area did not provide such information, constraining the authors to limit their comparison to those available in the literature.

9. CONCLUSION

In this paper, a full-wave method has been presented for an efficient characterization of the mixed coupling in multilayer bilateral microwave circuits including anisotropy. It can be applied to many structures in RF/microwave integrated circuits and in wireless communication systems. The efficiency of the spectral domain technique versus the application of Galerkin's technique was demonstrated through various examples. Adequate basis functions were found in hybrid mode for both odd and even modes. The computed time was also optimized to ensure a fast and accurate response. For three line bilateral couplers, neural networks models have been generated for effective permittivity and a very good agreement was found.

REFERENCES

1. Grzegorczyk, T. M., M. Nikku, X. Chen, B.-I. Wu, and J. A. Kong, "Refraction laws for anisotropic media and their application to left-handed metamaterials," *IEEE Transactions on Microwave Theory and Techniques*, Vol. 53, No. 4, April 2005.
2. Grzegorczyk, T. M., X. Chen, J. Pacheco Jr., J. Chen, B.-I. Wu, and J. A. Kong, "Reflection coefficients and Goos-Hanchen

shifts in anisotropic and bianisotropic left-handed metamaterials," *Progress In Electromagnetics Research*, PIER 51, 83–113, 2005.

3. Zhang, Y., X. Wei, and E. Li, "Electromagnetic scattering from three-dimensional bianisotropic objects using hybrid finite element-boundary integral method," *Journal of Electromagnetic Waves and Applications*, Vol. 18, No. 11, 1459, 2004.
4. Wu, B.-I., W. Wang, J. Pacheco, X. Chen, J. Lu, T. M. Grzegorczyk, J. A. Kong, P. Kao, P. A. Theophelakes, and M. J. Hogan, "Anisotropic metamaterials as antenna substrate to enhance directivity," *Microwave Opt. Technol. Lett.*, Vol. 48, No. 4, 680–683, Apr. 4, 2006.
5. Casula, G. A., G. Mazzarella, and G. Montisci, "Effective analysis of a microstrip slot coupler," *Journal of Electromagnetic Waves and Applications*, Vol. 18, No. 9, 1203, 2004.
6. Itoh, T., "Spectral domain approach for dispersion characteristics of generalized printed transmission lines," *IEEE Trans. on Microwave Theory and Tech.*, Vol. 28, 733–736, July 1980.
7. Radhakrishnan, K. and W. C. Chew, "Full-wave analysis of multiconductor transmission lines on anisotropic inhomogeneous substrates," *IEEE Trans. on Microwave Theory and Tech.*, Vol. 47, No. 9, 1764–1770, September 1999.
8. Mirshekar-Syahkal and D., J. B. Davies, "Accurate analysis of coupled strip-finline structure for phase constant, characteristic impedance, dielectric and conductor losses," *IEEE Trans. on Microwave Theory and Tech.*, Vol. MTT-30, No. 6, 906–910, June 1982.
9. Itoh, T. and A. S. Hebert, "A generalized spectral domain analysis for coupled suspended microstriplines with tuning septums," *IEEE Trans. on Microwave Theory and Tech.*, Vol. MTT-26, No. 10, 820–826, October 1978.
10. Kitazawa, T. and R. Mittra, "Quasi-static characteristics of asymmetrical and coupler coplanar-type transmission lines" *Ibid*, Vol. 33, 771–778, 1985.
11. Arai, S., et al., "A 900 MHz degree hybrid for QPSK modulator," *IEEE MTT-S Int. Microwave Symp. Dig.*, 679–682, 1991.
12. Tanaka, H., et al., "2-GHz one octave-band 90 degree hybrid coupler using coupled meander line optimized by 3-D FEM," *IEEE MTT-S Int. Microwave Symp. Dig.*, 906–906, 1994.
13. Tanaka, H., et al., "Miniaturized 90-degree hybrid coupler using high dielectric substrate for QPSK modulator," *IEEE MTT-S Int. Microwave Symp. Dig.*, 793–796, 1996.

14. Janiczak, B. J., "Multiconductor planar transmission-line structures for high directivity coupler applications," *IEEE MTT-S Int. Microwave Symp. Dig.*, 215–218, 1985.
15. Horno, M. and F. Medina, "Multilayer planar structures for high directivity directional coupler design," *Ibid*, 283–286, 1986.
16. Paolino, D. D., "MIC overlay coupler design spectral domain techniques," *IEEE Trans. on Microwave Theory and Tech.*, Vol. 26, 646–649, 1978.
17. Beyer, A. and K. Solbach, "A new fin-line ferrite isolator for integrated millimeter-wave circuit," *Ibid*, Vol. 29, 1344–1348, 1981.
18. Davis, L. E. and D. B. Sillars, "Millimetric coupled-slot finline components," *Ibid*, Vol. 34, 804–808, 1986.
19. Mu, T., H. Ogawa, and T. Itoh, "Characteristics of multiconductor asymmetric, slow-wave microstrip transmission lines," *Ibid*, 1471–1477, 1986.
20. Fukuoaka, Y., Q. Zhang, D. P. Neikirk, and T. Itoh, "Analysis of multilayer interconnection lines for high-speed digital integrated circuit," *Ibid*, Vol. 33, 527–532, 1985.
21. Itoh, T., "Spectral domain approach for calculating the dispersion characteristics microstrip lines," *IEEE Trans. on Microwave Theory and Tech., Ibid*, Vol. 21, 496–499, 1973.
22. Tounsi, M. L., R. Touhami, and M. C. E. Yagoub, "Fullwave analysis of bilateral microwave structures on multilayered uniaxially anisotropic substrate," *WSEAS Transactions on Electronics*, Vol. 1, No. 4, 621–626, Oct. 2004.
23. Ho, T. Q. and B. Becker, "Analysis of bilateral fin-lines on anisotropic substrates," *IEEE Trans. on Microwave Theory and Tech.*, Vol. 40, No. 2, 405–409, February 1992.
24. Ramakrishna, P. V. and D. Chadha, "Coupled mode analysis of finlines on anisotropic substrates," Department of Electrical Engineering Indian Institute of Technology, 1399–1400, August 10, 1989.
25. Sharma, A. K. and W. J. R. Hoefer, "Propagation in coupled unilateral and bilateral finlines," *IEEE Trans. on Microwave Theory and Tech.*, Vol. MTT-31, No. 6, 498–502, June 1983.
26. Kuo, J. T. and E. Shih, "Wideband bandpass filter design with three-line microstrip structures," *IEE Proc. Microw. Antennas Propag.*, Vol. 149, No. 5/6, 243–247, Oct./Dec. 2002.
27. Zhang, Q. J. and K. C. Gupta, *Neural Networks for RF and Microwave Design*, Artech House, Norwood, MA, 2000.
28. Patnaik, A., K. Mishra, G. K. Patra, and S. K. Dash, "An artificial

neural network model for effective dielectric constant of microstrip line," *IEEE Trans. Antennas Propagat.*, Vol. 45, 1697, Nov. 1997.

29. Zhang, Q. J., F. Wang, and M. S. Nakhla, "Optimization of high-speed VLSI interconnects: A review," *Int. J. Microwave Millimeter-Wave CAE*, Vol. 7, 83–107, 1997.
30. Horng, T., C. Wang, and N. G. Alexopoulos, "Microstrip circuit design using neural networks," *IEEE MTT-S Int. Microwave Symp. Dig.*, 413–416, Altanta, GA, June 1993.
31. Cho, C. and K. C. Gupta, "EM-ANN modeling of overlapping open-ends in multilayer microstrip lines for design of bandpass filters," *IEEE APS Int. Symp. Dig., Orlando, FL, July*, 2592–2595, Aug. 1999.
32. Zaabab, A. H., Q. J. Zhang, and M. S. Nakhla, "A neural network modeling approach to circuit optimization and statistical design," *IEEE Trans. Microwave Theory Tech.*, Vol. 43, 1349–1358, June 1995.
33. Biernacki, R., J. W. Bandler, J. Song, and Q. J. Zhang, "Efficient quadratic approximation for statistical design," *IEEE Trans. Circuits Syst.*, Vol. 36, 1449–1454, Nov. 1989.
34. Meijer, P., "Fast and smooth highly nonlinear multidimensional table models for device modeling," *IEEE Trans. Circuits Syst.*, Vol. 37, 335–346, Mar. 1990.
35. Zhang, Q. J., "NeuroModeler," Department of Electronics, Carleton University, 1125 Colonel By Drive, Ottawa, Canada, K1S 5B6.